

Stepwise Separation for Calcium Recovery from an Ammonium Sulfate Leaching System

Wenxiu Li, Yongzheng Gu, Yuhang Yang, Tao Wang,* and Mengxiang Fang



Cite This: *Ind. Eng. Chem. Res.* 2023, 62, 5181–5189



Read Online

ACCESS |



Metrics & More

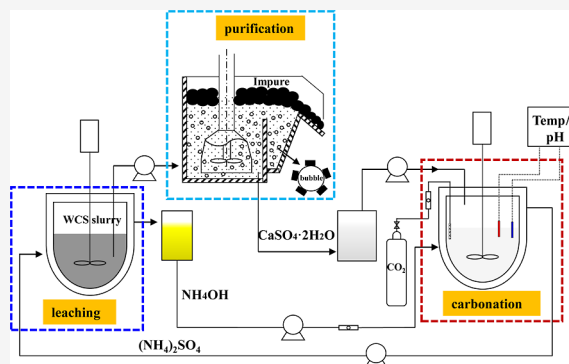


Article Recommendations



Supporting Information

ABSTRACT: Calcium recovery from high calcium solid waste is driven by the latter's growing environmental impact, emphasizing the need to develop a high value-added utilization approach. Inspired by our previous study, we develop a stepwise separation strategy for calcium recovery from an ammonium sulfate leaching system to efficiently remove iron and unburned carbon residue. In this study, tributyl phosphate (TBP) used as the carbon residue adsorbent for calcium recovery exhibits high selectivity and good recycling stability. Adsorption measurements show that TBP yields a superior carbon residue adsorption ability with a maximum adsorption ratio greater than 95%. Moreover, the adsorption percentage is also kept more than 90% after 10 cycles, which substantiates the good potential of TBP for reuse. Besides, the low concentration (1 mol/L) of H_2SO_4 provides an acidic environment, which makes TBP more feasible to be applied in carbon residue adsorption and effective iron(III) stripping. Furthermore, it is inferred from the Fourier transform infrared spectroscopy/X-ray photoelectron spectrometer and density functional theory analyses that the enhanced carbon separation performance may be ascribed to the carboxyl in carbon residue coordinated to the donor oxygen atom of TBP at the position of P–O. This work provides the foothold for further research on the recovery of calcium from industrial by-products.



1. INTRODUCTION

Waste carbide slag (WCS) is a by-product of polyvinyl chloride (PVC), and long-term piling in the open air causes serious environmental pollution.^{1,2} Given that it consists of 90% CaO, many studies^{3,4} have been conducted to explore its applicability as a calcium source for synthetic calcium carbonate (CaCO_3). It was well established that ammonium sulfate ($(\text{NH}_4)_2\text{SO}_4$), a recyclable WCS leaching agent, made the calcium undergo “ $\text{CaSO}_4\text{--CaCO}_3$ ” multiple phase transitions throughout the whole process, which was beneficial to regulating the CaCO_3 crystallization with a narrow particle size distribution.⁵ However, the impurities, especially the unburned carbon residue and iron(III) in WCS, also coexist in the crystalline phases and significantly affect the whiteness and purity of CaCO_3 . Therefore, the deep separation of unburned carbon residue and iron(III) is essential to recycling and resource utilization of WCS. Many attempts have been made to remove unburned carbon residue and iron(III), such as froth flotation or adsorption of unburned carbon in mineral processing^{6–8} and chemical precipitation or extraction of iron(III) from the adsorption systems.^{9,10}

Unburned carbon residue in WCS represents the main factor restricting the whiteness of the product. Generally, it is processed via burning, and high temperature is costly with large amounts of energy consumed. An economical and efficient physical and chemical method has huge prospects for large-scale industrial applications to avoid additional roasting

energy consumption. It has been shown that the conventional flotation method can significantly strip unburned carbon through bubble adsorption. Zhang et al.¹¹ reported that most of the fine slag was not polymerized in the carbon residue, and froth flotation could be realized for separation. It is also found that reverse flotation yields a superior separation effect than positive flotation. The composite collectors containing AC1201 and kerosene could effectively separate fine carbon residue, but the content of tailings did not exceed 90%.⁸ However, the entrainment of reagents remains a critical issue, resulting in high collector consumption and low recovery ability.^{12,13} In addition, iron(III) is another major impurity that directly affects the performance of final CaCO_3 products. Increasing evidence^{14,15} suggest that the solvent adsorption method based on tributyl phosphate (TBP) is suitable for iron removal. The adsorbent containing 12.5 vol % TBP and 87.5 vol % kerosene exhibits satisfying adsorption of Fe^{3+} from raw phosphoric acid. Notably, in the $(\text{NH}_4)_2\text{SO}_4$ leaching system, over 90% of the calcium in WCS is first extracted into the

Received: September 14, 2022

Revised: February 9, 2023

Accepted: March 2, 2023

Published: March 13, 2023



insoluble $\text{CaSO}_4 \cdot 2\text{H}_2\text{O}$. Accordingly, chemical precipitation cannot fully separate iron(III) and calcium components. Based on the inspiration of the froth flotation principle, unburned carbon can be adsorbed by organic reagents and stripped through phase separation. Therefore, emphasis should be placed on selecting organic solvents that can effectively adsorb unburned carbon. It is well recognized that unburned carbon is hydrophobic, and the adsorption process is commonly enhanced using solvents with hydrophobic and non-ionic hydrophilic groups.¹⁶ Indeed, conventional oils such as kerosene, fuel oil, and waste oil¹⁷ exhibit good adsorption performance in low-rank coal systems. However, the relatively low unburned carbon content in the suspension system leads to weak adsorption ability under the same conditions. It has been shown that TBP also has a certain adsorption effect on unburned carbon particles. Moreover, current evidence¹⁸ suggests that the presence of iron ions is beneficial in enhancing the adsorption of other substances from the acidic system by TBP. Therefore, synergistic adsorption of unburned carbon by iron-loaded TBP in a sulfate suspension system represents a cost-effective approach to removing unburned carbon and iron impurities. In addition, since the detailed adsorption process, including the adsorption site of unburned carbon, cannot be directly observed, the density functional theory (DFT) calculation on the adsorption mechanism is implemented. It has been reported that DFT simulation can visually clarify the adsorption mechanism between the solvent and metal ions.^{14,18} However, the effect of functional groups of carbonaceous surfaces on the adsorption mechanism is rarely mentioned. Therefore, it is necessary to figure out the adsorption mechanism of TBP on the carbon surface by DFT simulation.

In this work, TBP is used for calcium recovery from the $(\text{NH}_4)_2\text{SO}_4$ leaching system, and the influencing factors, including concentration and phase ratio on the unburned carbon adsorption behavior, are systematically studied. Additionally, a certain amount of H_2SO_4 solution is employed to adjust the pH value of the system, which can not only remove the iron(III) by solid–liquid separation but can also convert CaCO_3 from raw materials into the desired $\text{CaSO}_4 \cdot 2\text{H}_2\text{O}$. Furthermore, the DFT method is employed to better understand the adsorption mechanism of carbon residues. Finally, to better reveal the underlying adsorption mechanism, the effect of the type of functional groups in the carbon structure on the adsorption is determined using molecular electrostatic potential (MEP) and adsorption energy based on DFT calculation.

2. EXPERIMENTAL SECTION

2.1. Materials. WCS is obtained from Beiyuan Chemical Group Co., Ltd., Shanxi, China. The chemical components are determined by X-ray fluorescence (Panalytical) and thermogravimetric analysis (TGA, Mettler), and the results are listed in Table 1. More than 80% of calcium components are detected in WCS, and the remaining 11.16% is mainly attributed to unburnt carbon residue and iron(III). The adsorbent of TBP is

Table 1. Chemical Components of Waste Carbide Slag (wt %)

sample	CaO	Ca(OH) ₂	CaCO ₃	Fe ₂ O ₃	SiO ₂	Al ₂ O ₃	C
WCS	83.0	73.38	9.23	4.78	3.7	1.31	6.38

purchased from Macklin, and the chemical structure is exhibited in Figure 1. The adsorbent is prepared by mixing

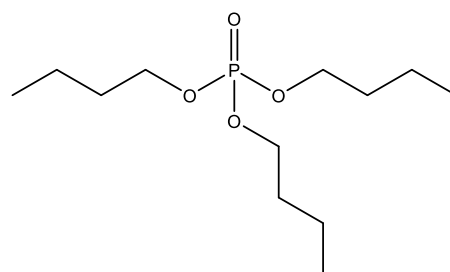


Figure 1. Chemical structure of tributyl phosphate.

TBP and sulfonated kerosene at the designed volume ratio in a 500 mL volumetric flask. 98% sulfuric acid (H_2SO_4) is purchased from the China National Pharmaceutical Group Corporation. Ultrapure water (conductivity $\leq 10^{-4} \text{ S m}^{-1}$) is used for the experiment and chemical analysis. All chemical reagents are used without further purification.

2.2. Separation and Purification. As shown in Figure 2, to prevent impurities from being wrapped by the leaching

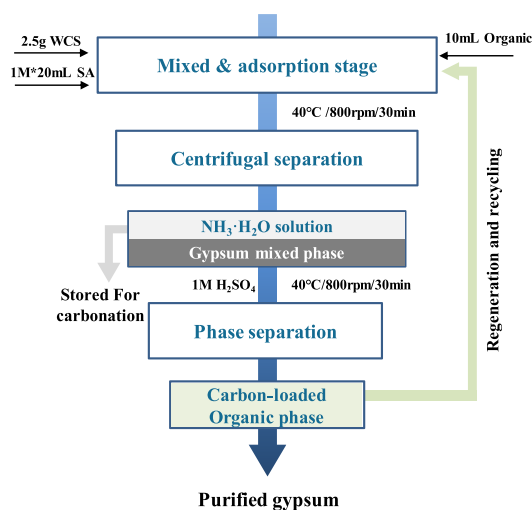


Figure 2. Flow sheet of the impurity separation and recycling of the adsorbent.

product (gypsum), the extraction process was conducted by simultaneously mixing WCS, $(\text{NH}_4)_2\text{SO}_4$ solution, and organic phase (TBP) in a 50 mL centrifuge tube. Then, the mixture was stirred vigorously in a thermostatic heating magnetic stirrer at the desired temperature. The reaction was conducted for 30 min to ensure that the adsorption achieved equilibrium. After centrifugation, the aqueous solution phase (NH_4OH) was separated and stored for further carbonation. Subsequently, 1 mol/l of H_2SO_4 was added dropwise to the raffinate phase to adjust equilibrium pH values. During this process, iron(III) was converted into Fe^{3+} aqueous solution, and the weathered CaCO_3 from raw material could be completely removed without introducing new impurities. After continuous stirring for 30 min, the suspension was transferred to a separatory funnel for the final phase separation. The solid–liquid mixed phase in the lower layer was filtered, and the precipitate was washed using distilled water and then dried at 65°C for 24 h. In contrast, the organic phase loaded with the

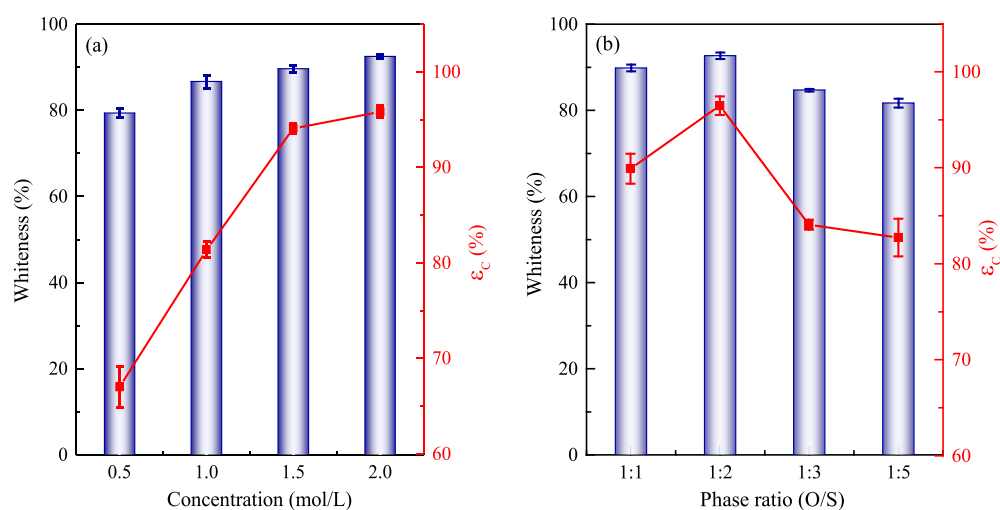


Figure 3. Adsorption performance under different conditions: (a) concentration and (b) phase ratio.

carbon residue was desorbed using deionized water, and the organic solvent was fed back to the leaching step for the next recycling.

The amount of iron in the leaching residue was then identified by chemical analysis [inductively coupled plasma optical emission spectroscopy (ICP-OES)], and the contents of carbon before and after adsorption were determined by an elemental analyzer vario EL cube. The extractive ratio of iron and carbon was calculated according to the following equation

$$\epsilon_{\text{Fe/c}} = \left(1 - \frac{m_i \times w_i}{m_0 \times w_1} \right) \times 100\%$$

where m_i is the weight of the leached residue after extraction equilibrium, mg; w_i is the amount of iron or carbon in the leached residue, %; m_0 is the initial mass of WCS, mg; and w_1 is the amount of iron or carbon in raw materials, %.

2.3. Characterization and Analysis. The infrared spectra before and after adsorption were measured by Fourier transform infrared (FTIR) spectroscopy with attenuated total reflection accessories (Tensor-27, Bruker). An inductively coupled plasma optical emission spectrometer (Thermo Fisher ICP 6000, USA) was used to detect the concentration of iron(III) in the solutions. The micromorphology was captured before and after adsorption using a scanning electron microscope (SU-8010, Hitachi) under an accelerating voltage of 3 kV (Beam Current: 0.1 nA, Spot Size: 30). The X-ray photoelectron spectroscopy measurements were obtained using a Thermo Scientific ESCALAB 250Xi X-ray photoelectron spectrometer (XPS, USA). C 1s peak at 284.6 eV was applied to compensate for the surface charge effects of binding energies. A digital pH meter (Rex PHS-3C, China) was used to monitor the pH of the suspension with an accuracy of ± 0.01 PH. Moreover, the contents of CaCO_3 in gypsum before and after acidification were measured by TGA (Mettler).

2.4. DFT Calculation. In this work, the DFT, which provided a good balance between calculation efficiency and accuracy,^{19–21} was applied to calculate structural properties. All DFT calculations were performed with the Forcite program package of Materials Studio software. The COMPASS force field was used to model the interactions between the adsorbent (TBP) and oxygen-containing functional group in carbon residues, including van der Waals and the Coulomb

interactions. The simulations were performed using the Nose–Hoover thermostat and NVT ensemble with a time step of 1 fs.²² Besides, periodic boundary conditions were used to avoid the influence of boundary or finite size. Every adsorption model was set with rigid characteristics, which meant that bond lengths and angles were fixed. The outer surface of the crystals and surface effects were also neglected in the simulations. It has been shown that carbon rings from a single-layer graphite structure were successfully applied to simulate carbonaceous surface models.²³ In the current work, different oxygen-containing functional groups were constructed based on graphite to investigate the adsorption characteristics of TBP on the surface of the functional oxygen group. The relative electron density is an important index in adsorption, and the MEP (ESP) calculations were carried out in the GAUSSIAN program package. For geometry optimization calculations, the B3LYP functional²⁴ and def2-SVP basis set²⁵ were used, and the optimal geometry for each compound was determined.

The adsorption energy (E_{bind}) was an important index to evaluate the adsorption process, and the interaction energy was calculated by the following formula

$$E_{\text{bind}} = E_{\text{complex}} - (E_A + E_B)$$

where E_{complex} is the total energy of TBP and the carbon residue model in the equilibrium state, E_A is the energy of a single TBP molecule, and E_B is the energy of the carbon residue model.

3. RESULTS AND DISCUSSION

3.1. Adsorption of Carbon Residue. The whiteness of $\text{CaSO}_4 \cdot 2\text{H}_2\text{O}$ is directly related to further utilization and application. In this system, the carbon residue is the main component that affects the whiteness, and it is found in $\text{CaSO}_4 \cdot 2\text{H}_2\text{O}$ in two possible forms: (1) attached to the surface of $\text{CaSO}_4 \cdot 2\text{H}_2\text{O}$ and (2) wrapped in CaCO_3 that is formed by natural weathering. Notably, the wrapped carbon residue is completely exposed in the $\text{CaSO}_4 \cdot 2\text{H}_2\text{O}$ suspension along with the addition of H_2SO_4 solution. Here, the organic solvent (TBP) is employed to extract the carbon residue from the $\text{CaSO}_4 \cdot 2\text{H}_2\text{O}$ suspension. The carbon adsorption ratio (ϵ) is widely acknowledged as an important index of the adsorption process for carbon separation. Besides, the

whiteness of the purified $\text{CaSO}_4 \cdot 2\text{H}_2\text{O}$ is evaluated. As shown in Figure 3, the adsorption ratio of the carbon residue with different concentrations of adsorbents is studied systematically. The adsorbents ranging from 0.5 to 2.0 mol/L are prepared by TBP dissolved in sulfonated kerosene.²⁶ We find that 0.5–1.5 mol/L TBP yields a significant adsorption effect on the carbon residue. As shown in Figure 3a, TBP exhibits a relatively excellent adsorption performance, and the carbon adsorption ratio reaches 95.6% with 2.0 mol/L TBP. A study²⁷ showed that TBP had a relatively good adsorption sensitivity in acidic circumstances, suggesting that the H_2SO_4 solution enhanced the adsorption behavior to a certain extent. Additionally, it can be seen that the initial whiteness of the produced $\text{CaSO}_4 \cdot 2\text{H}_2\text{O}$ is less than 80%, while the purified $\text{CaSO}_4 \cdot 2\text{H}_2\text{O}$ is increased to 93%, which can meet the requirements for further applications. The effects of phase ratio (O/S) from 1:1 to 1:5 is also investigated to better understand adsorbent consumption during adsorption. As shown in Figure 3b, a lower dosage of organic solvents is not conducive to carbon adsorption. The relative superior adsorption performance of 96% is obtained at an O/S of 1:2, yielding purified $\text{CaSO}_4 \cdot 2\text{H}_2\text{O}$ with 93% whiteness. The relatively high dosage of organic solvents can not only provide more contact chance between carbon and the active site of TBP but can also supply the driving force to overcome the resistance of mass transfer, leading to an increase in carbon uptake.^{26,27} When the organic phase ratio is further decreased to 1:5, the carbon adsorption ratio steeply decreases to 80%. Correspondingly, the whiteness of purified $\text{CaSO}_4 \cdot 2\text{H}_2\text{O}$ shows the same tendency. Based on the above analysis, TBP with an optimum phase ratio of 1:2 is adopted in the subsequent experiments.

3.2. Removal of Iron(III). In addition, it is widely acknowledged that iron(III) exists as Fe^{3+} at a certain concentration in an acidic system. Figure 4 shows the effect

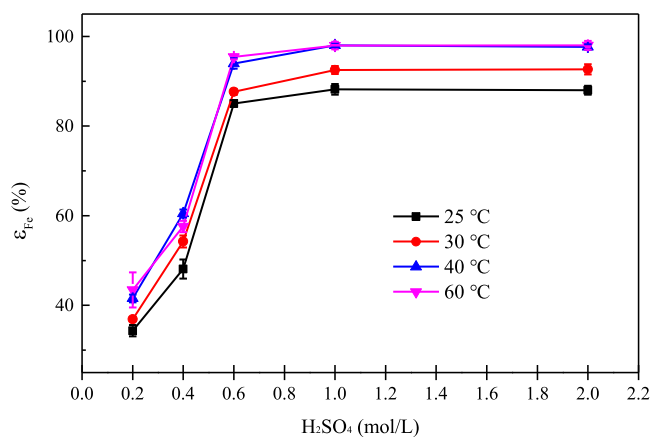


Figure 4. Effect of H_2SO_4 concentration on iron(III) removal.

of H_2SO_4 concentration ranging from 0.2 to 2.0 mol/L on iron(III) removal at 30–60 °C. It can be seen that the stripping ratio of iron(III) is increased with the increase of H_2SO_4 concentration, and the maximum stripping capacity is achieved in the range of 0.6–1.0 mol/L. Meanwhile, the iron(III) stripping ratio increases with the increase of temperature, and more than 95% of iron(III) can be removed at a temperature of 40 °C. Notably, due to weathered CaCO_3 in WCS, the calcium source in the raw material could not be fully converted into the desired calcium product (CaSO_4

$2\text{H}_2\text{O}$) in this leaching system. Besides, at further stage of $\text{CaSO}_4 \cdot 2\text{H}_2\text{O}$ carbonation, the formation of final calcium carbonate undergoes two critical processes: nucleation and crystallization. The existence of weathered CaCO_3 affects the crystal growth of the final calcium carbonate, which is not conducive to the particle size control of the final calcium carbonate. Therefore, the addition of a low-concentration H_2SO_4 solution can not only remove impurities from iron(III) but also contribute to converting weathered CaCO_3 into the desired $\text{CaSO}_4 \cdot 2\text{H}_2\text{O}$.

To further determine the influence of H_2SO_4 concentration on the weathered CaCO_3 dissolution, Figure 5 shows the TGA analysis of the acidified products. It can be clearly seen that there is an obvious weight loss in the temperature range of 100–200 °C, which is caused by the weight loss of the crystal water of gypsum, and the corresponding content of $\text{CaSO}_4 \cdot 2\text{H}_2\text{O}$ is also increased with the increase of H_2SO_4 concentration. However, the weight loss using 2.0 mol/L H_2SO_4 solution is lower than that of the 1.0 mol/L solution, indicating that the mixed crystalline phases ($\text{CaSO}_4 \cdot 0.5\text{H}_2\text{O}/\text{CaSO}_4 \cdot 2\text{H}_2\text{O}$) of calcium sulfate are formed (crystalline phase results in Figure S1). In our previous study,⁵ the crystal phase of $\text{CaSO}_4 \cdot 2\text{H}_2\text{O}$ was the key product that affected the crystallization of nano-sized CaCO_3 . Therefore, a higher H_2SO_4 concentration is not recommended because the acidified product is changed. Besides, another obvious weight loss is also observed in the temperature range of 550–750 °C, which is attributed to the decomposition of weathered CaCO_3 . From the TGA curve, it can be visually seen that the weight loss peak of weathered CaCO_3 gradually disappears with the increase of H_2SO_4 concentration. Furthermore, according to the pie chart of the CaCO_3 content, the concentration range of 0.6–1.0 mol/L can effectively remove the weathered CaCO_3 , which also explains the reason why the iron(III) stripping ratio is slowly increased when the H_2SO_4 solution is 0.6–1.0 mol/L.

Moreover, Figure 6 shows the purity and whiteness indexes of the calcium leaching product ($\text{CaSO}_4 \cdot 2\text{H}_2\text{O}$) before and after impurity separation. It can be seen that the whiteness of $\text{CaSO}_4 \cdot 2\text{H}_2\text{O}$ is increased from 78 to 93%, and its purity is also increased to about 93.5% after decarburization. Finally, after further dissolution and acidification of iron(III) impurities with 1.0 mol/L H_2SO_4 solution, about 95.5% purity and 95% whiteness of $\text{CaSO}_4 \cdot 2\text{H}_2\text{O}$ are obtained. Furthermore, we compare and analyze both the purity and whiteness indexes of $\text{CaSO}_4 \cdot 2\text{H}_2\text{O}$ obtained from pure calcium hydroxide (99.999%) under same leaching conditions. It can be clearly seen that after impurity separation and purification, both the purity and whiteness indexes of $\text{CaSO}_4 \cdot 2\text{H}_2\text{O}$ leached from WCS are similar to those of pure calcium hydroxide, which can fully meet the requirements of the calcium source for the next carbonation stage.

3.3. Adsorption Mechanism. It is well established that the $\text{CaSO}_4 \cdot 2\text{H}_2\text{O}$ precipitate is insoluble, and the micro-structural characteristics of $\text{CaSO}_4 \cdot 2\text{H}_2\text{O}$ and attached impurities can be visually observed by SEM–EDX analysis. As seen in Figure 7a, the particles of $\text{CaSO}_4 \cdot 2\text{H}_2\text{O}$ exhibit a rod-like shape with a length of up to 10 μm , covered by a large number of fine particles. Correspondingly, the content of main elements Ca, O, and S from EDX analysis further confirms the formation of $\text{CaSO}_4 \cdot 2\text{H}_2\text{O}$, while the elements of Al, O, C, and Si with lower amounts are ascribed to impurities. After adsorption, the surface of $\text{CaSO}_4 \cdot 2\text{H}_2\text{O}$ crystals is smooth, and the small particles attached are completely cleaned out (Figure

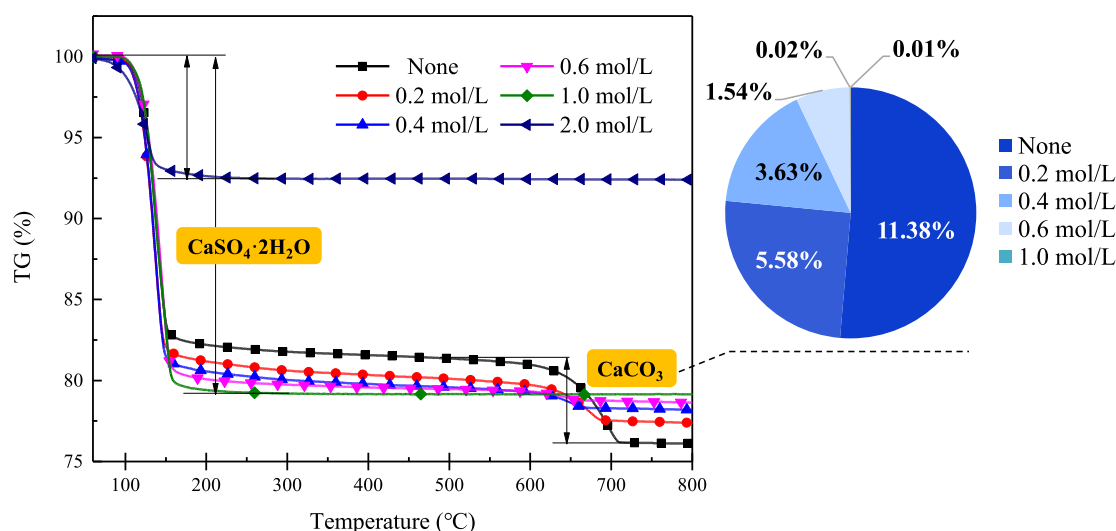


Figure 5. TG analysis of the acidified products.

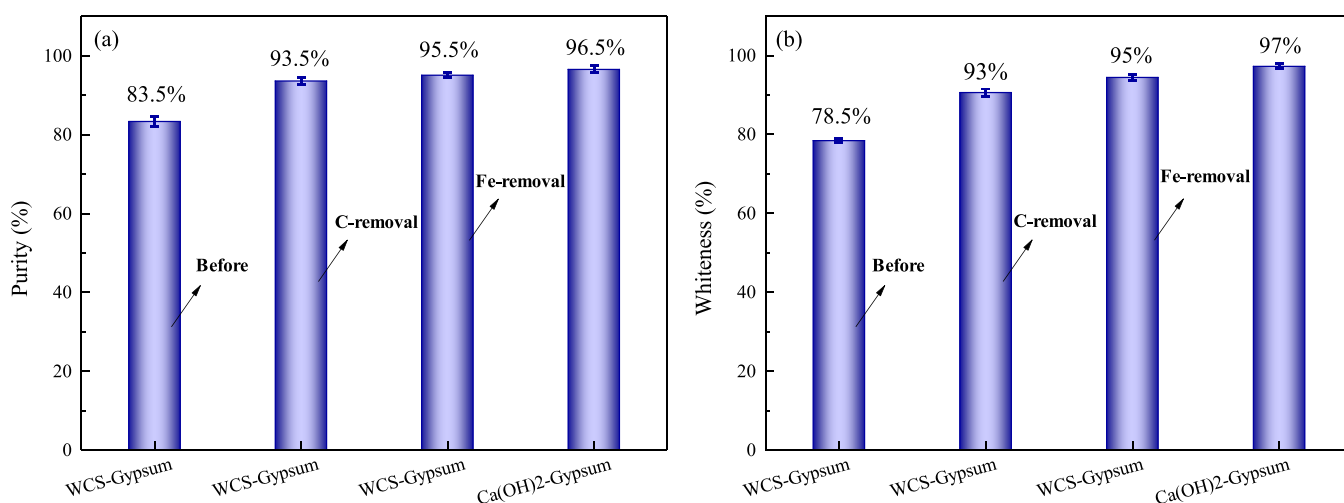


Figure 6. Purity and whiteness of the gypsum products: (a) purity and (b) whiteness.

7b). Additionally, the EDX results show that a majority of impure elements are separated, indicating that both CaCO_3 and carbon residues in the leached product are effectively removed.

Furthermore, FTIR spectroscopy is employed to gain further insights into functional group changes before and after adsorption. In Figure 8, absorption in the range $3000\text{--}2800\text{ cm}^{-1}$ belongs to C–H stretching vibration and the peaks at $1500\text{--}1340\text{ cm}^{-1}$ are ascribed to C–H and $-\text{CH}_3$ bending vibrations of the alkyl group of TBP. The absorption peak at 1265 cm^{-1} is attributed to the P=O stretching vibration for TBP. The stretching vibration of the P–O–C group corresponds to the peaks at 1020 and 981 cm^{-1} .^{14,27,28} Notably, the absorption peak of the P=O bond appearing at 1265 cm^{-1} is still present after adsorption, indicating no strong interactions between the P=O group and the carbon residue. The most significant change is the shift of the P–O–C vibration peak, probably owing to the formation of a coordination interaction. However, the single-bonded oxygen normally exhibits a weaker polarity than the double-bonded oxygen. Thus, it is preliminarily inferred that the possible interaction site between TBP and the carbon residue during

the adsorption process may occur in the vicinity of the P–O–C group.

To further figure out which carbon functional groups in the carbon residue interact with TBP, the XPS spectra of solid phases before and after adsorption are also recorded. The XPS survey spectra presented in Figure 9a show that three strong peaks at about 530.9, 347.8, and 169.2 eV correspond to O 1s, Ca 2p, and S 2p, respectively, indicating that $\text{CaSO}_4\cdot 2\text{H}_2\text{O}$ is the main component. Notably, the C1s peak in the purified product at about 284 eV shows a lower intensity, suggesting that TBP is beneficial for removing carbon impurities in $\text{CaSO}_4\cdot 2\text{H}_2\text{O}$. Moreover, the C 1s XPS spectrum is fitted as four vibration satellite peaks using the Gaussian fitting method. The peaks at 284.8 and 285.7 eV are attributed to C–C/C–H and C–O groups. The remaining two peaks at 287.2 and 289.2 eV are assigned to C=O/O=C–O (in low-rank coals) and COO^- groups, respectively.²⁹ Table 2 shows the relative contents of carbon-containing groups of the C 1s peak corresponding to C–C/C–H, C–O, C=O/O=C–O, and COO^- . Combined with Figure 9b,c, it is obvious that the content of the carboxyl group decreases after adsorption. This phenomenon may be ascribed to the strong interactions between carboxyl in the carbon residue and TBP at the

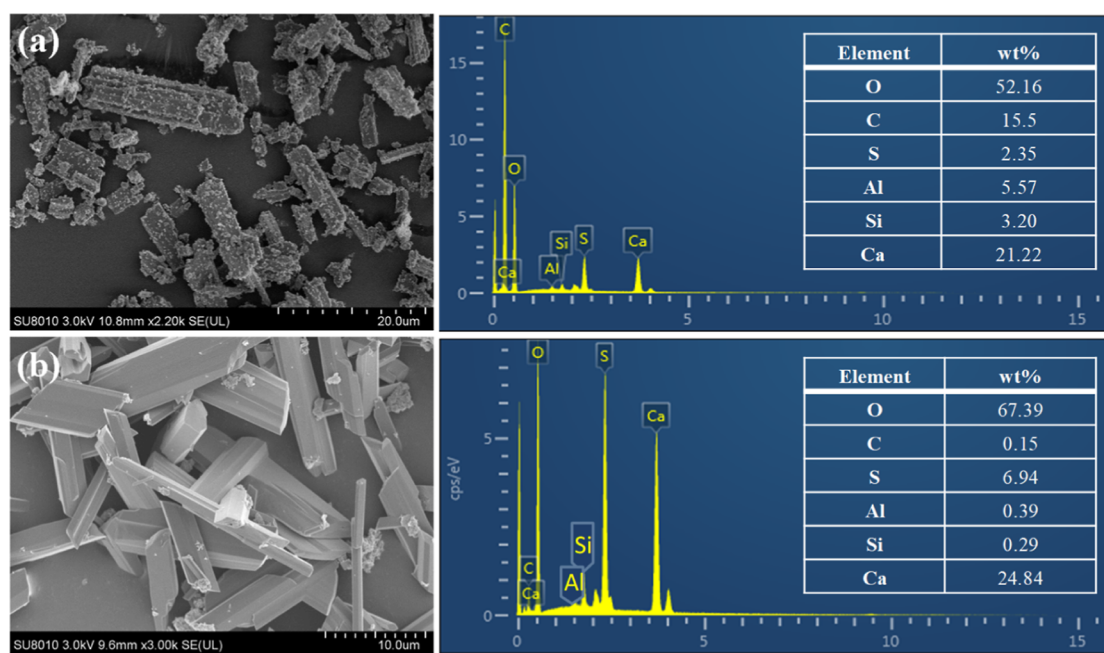


Figure 7. SEM analysis of the purified products (a) before and (b) after adsorption.

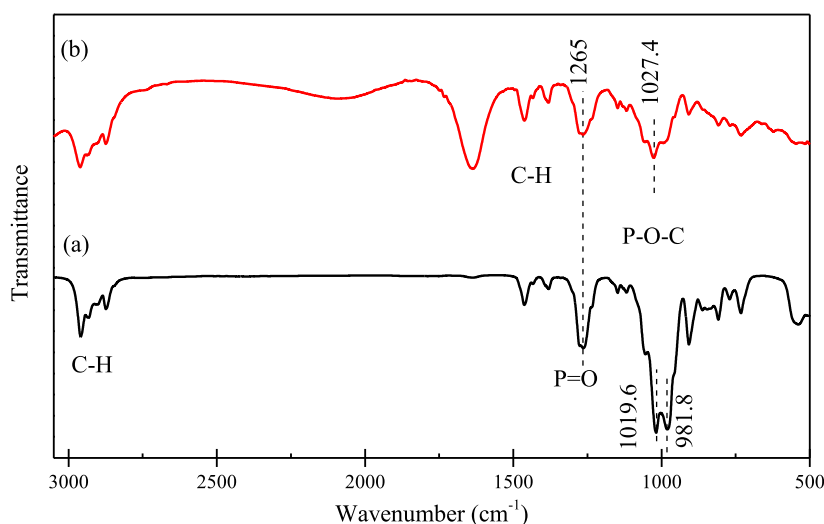


Figure 8. FTIR analysis of the purified products (a) before and (b) after adsorption.

position of the P–O–C/P=O group, leading to the effective separation of the carbon residue from the precipitated $\text{CaSO}_4 \cdot 2\text{H}_2\text{O}$. In addition, the relative amounts of C–C/C–H (284.8 eV) and C–O (285.7 eV) are slightly higher, which may be related to the C–C/C–H and C–O groups in TBP.

3.4. DFT Calculation. We employ molecular dynamics simulations based on FTIR and XPS analyses to further determine the interaction sites between TBP and organic functional groups in the carbon residue. Figure S3 shows the optimal structure and equilibrium structure of the TBP molecule and the low order carbon model grafted with different oxygen groups. It can be observed that TBP molecules are mainly adsorbed on the surface of carboxyl and ester groups in a planar configuration after optimization calculation. The bond length of carbon–carbon bond or carbon–oxygen bond connected with the carboxyl group and ester group has deviated after optimization calculation. Besides, the carboxyl group is closer to the TBP molecule, which is

basically consistent with the result of XPS analysis. It is indicated that the TBP molecule has a significant effect on the adsorption configuration of the low order carbon structure on the surface of the carboxyl group. Moreover, it can be seen from Table S1 that the adsorption energy (E_{bind}) between TBP and the carboxyl group (0.76 eV) is higher than that of the ester group (0.55 eV), which indicates that there is a relatively large interaction force between TBP and the carboxyl group, making TBP more likely to occupy the adsorption site.³⁰

Furthermore, the probability of carboxyl at a certain distance from TBP is calculated by the radial distribution function (RDF). As seen in Figure 10, the graph features plenty of sharp peaks, indicating that the probability of occurrence for the particles is relatively fixed in some positions and particles exhibit a well-arranged distribution.³¹ In addition, information on the interaction of atoms between TBP and the carbon residue model is acquired using RDFs.^{22,32} In our study, intermolecular hydrogen bonding is adopted to characterize

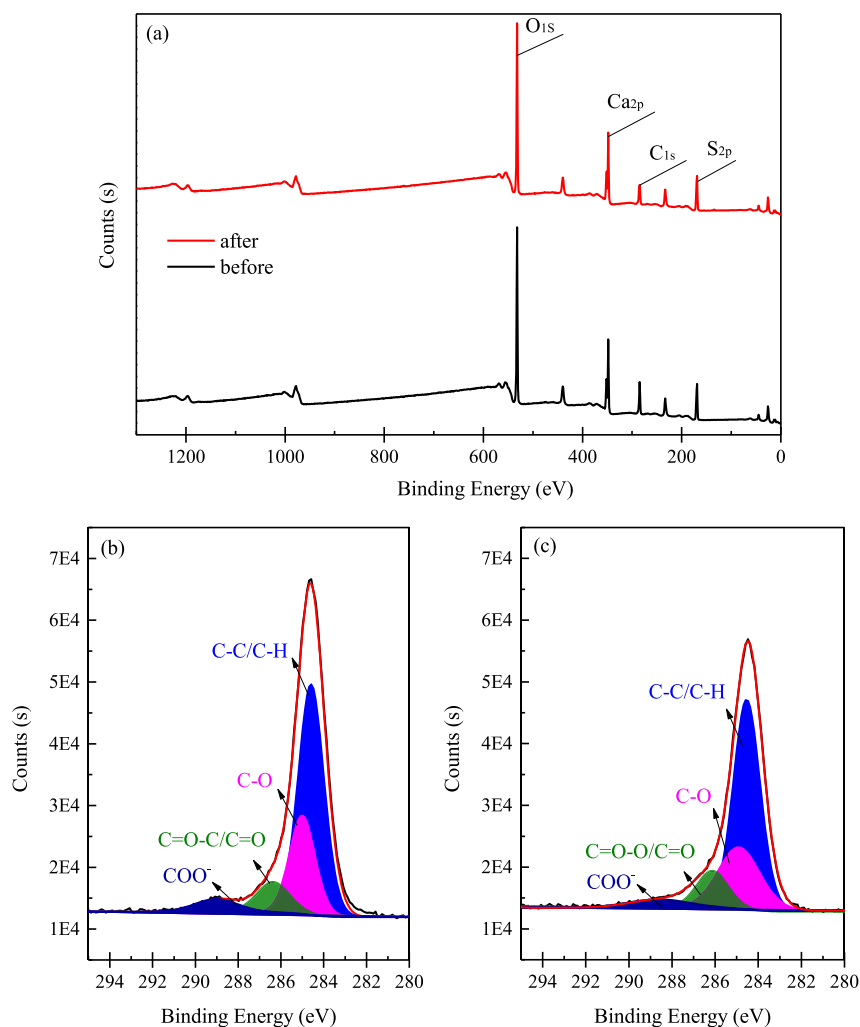


Figure 9. (a) XPS full spectra scans before and after adsorption; (b) C 1s XPS spectra before adsorption; (c) C 1s XPS spectra after adsorption.

Table 2. Classification and Relative Content of the Organic Carbon of Samples

sample	C-H/C-C	C-O	C=O/O=C=O	COO ⁻
before	55.13	24.77	11.85	9.11
after	57.97	26.52	10.99	4.01

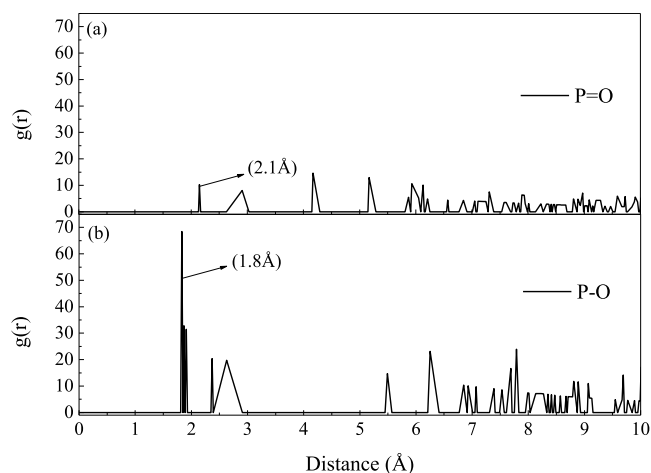


Figure 10. RDF for: (a) carboxyl H-TBP double bond O and (b) carboxyl H-TBP single bond O.

intermolecular interactions. The established cutoff distance between intermolecular oxygen and hydrogen of 2.45 Å is often used to demonstrate the presence of hydrogen bonding.²² As shown in Figure 9, the single bond oxygen atom in TBP is coordinated to the hydrogen atoms of carboxyl in the carbon residue model, and a relatively sharp peak is observed at 1.8 Å. It can be inferred that strong hydrogen bonds are formed between the carboxyl group and the TBP molecule. Furthermore, the peak intensity of the single bond oxygen-carboxyl system reaches 70. Correspondingly, the distances between double bond oxygen atoms in TBP and hydrogen atoms of carboxyl fall within the cutoff range, verified by the peaks at approximately 2.1 Å in RDFs. However, the peak intensity of the double bond oxygen-carboxyl system is relatively weak, indicating weak or no hydrogen bonding interaction. Based on the above analysis, the interaction sites between TBP and the carbon residue organic functional group are more likely to occur at the position of P-O, which is in accordance with the results of the FTIR analysis.

The MEP (ESP) can be used to predict the partial reactivity of the molecule. Figure 11 shows the ESP map of the formed complex structure and the color associated with the charge density. Herein, blue areas are positively charged and red or orange areas are negatively charged. It can be clearly seen that this system is a combination of electropositive and neutral

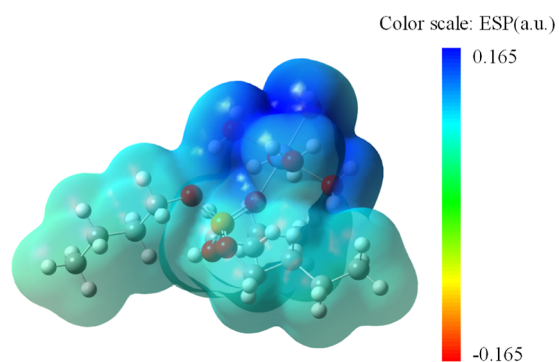


Figure 11. ESP map of the $[\text{TBP Fe (H}_2\text{O)}_6]$.

fragments. The TBP displaying an electric neutrality spot center on the $\text{P}=\text{O}$ functional group has a trend to absorb the electropositive spots associated with $[\text{Fe (H}_2\text{O)}_6]^{3+}$ cation. Additionally, the light-green areas surrounding TBP indicate that the interaction with iron ions may occur through electron clouds generated by the sp_2 hybridization orbital.^{33,34}

3.5. TBP Cyclic Capacity. It is a necessary step to reuse the adsorption capacity of TBP, so the recycling performance of TBP is also evaluated (Figure 12). The result shows that the carbon adsorption ratio remains around 90% after TBP cycling five times. Subsequently, the carbon adsorption ratio decreases by $\sim 20\%$, and the whiteness of $\text{CaSO}_4 \cdot 2\text{H}_2\text{O}$ correspondingly decreases to 80% in the 10th cycle. These findings indicate that TBP is a promising adsorbent for the selective separation of the carbon residue in this system, and more work is needed to improve the recycling ability for long-term use.

4. CONCLUSIONS

In this work, we have proposed a stepwise calcium separation method from an $(\text{NH}_4)_2\text{SO}_4$ leaching system. The results show that nearly 96% of the carbon residue can be removed under the optimal conditions of 2.0 mol/L TBP and phase ratio of 1:2. Meanwhile, more than 95% of iron(III) can be stripped at a temperature of 40 °C with 1 mol/L H_2SO_4 solution. Correspondingly, the 95.5% purity of $\text{CaSO}_4 \cdot 2\text{H}_2\text{O}$ with a

whiteness of 95% is effectively separated. Furthermore, the adsorption performance between TBP and the carbon residue at the atomic level shows that the strong interaction forces between TBP and the carboxyl group make it easier to occupy more chemisorption sites on the surface. The recycle ability of TBP in subsequent adsorption shows that the adsorption percentage remains more than 90% after 10 cycles. The convenient regeneration of TBP further confirms the feasibility of this method in industrial applications.

■ ASSOCIATED CONTENT

SI Supporting Information

The Supporting Information is available free of charge at <https://pubs.acs.org/doi/10.1021/acs.iecr.2c03312>.

XRD analysis of the acidified products; detailed model construction of TBP adsorption carbon structure; and optimized molecular structure of carboxyl and ester (PDF)

■ AUTHOR INFORMATION

Corresponding Author

Tao Wang – State Key Laboratory of Clean Energy Utilization and Key Laboratory of Clean Energy and Carbon Neutrality of Zhejiang Province, Zhejiang University, Hangzhou 310027, PR China; orcid.org/0000-0001-9277-4027; Email: ootgnaw@zju.edu.cn

Authors

Wenxiu Li – State Key Laboratory of Clean Energy Utilization and Key Laboratory of Clean Energy and Carbon Neutrality of Zhejiang Province, Zhejiang University, Hangzhou 310027, PR China

Yongzheng Gu – GD Power Development Co., Ltd., Beijing 100101, PR China

Yuhang Yang – State Key Laboratory of Clean Energy Utilization and Key Laboratory of Clean Energy and Carbon Neutrality of Zhejiang Province, Zhejiang University, Hangzhou 310027, PR China

Mengxiang Fang – State Key Laboratory of Clean Energy Utilization and Key Laboratory of Clean Energy and Carbon

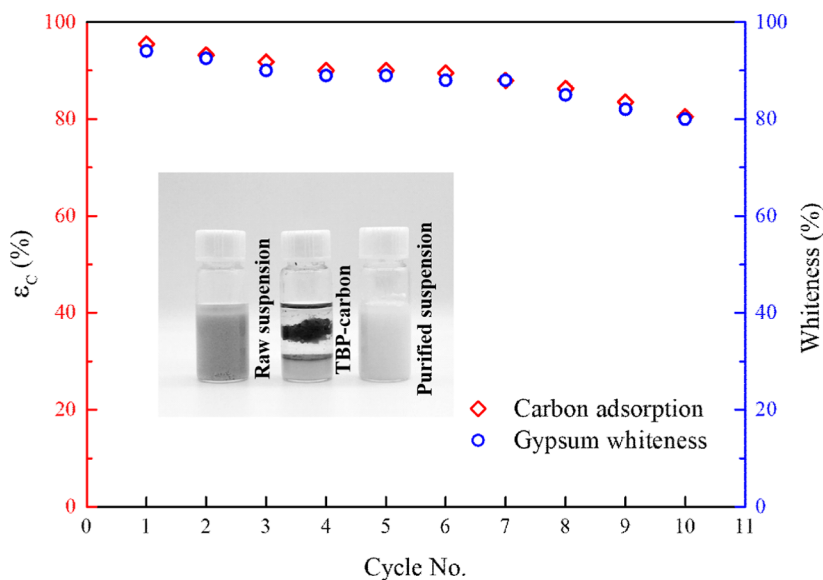


Figure 12. Reusability of TBP for the adsorption of calcium.

Neutrality of Zhejiang Province, Zhejiang University,
Hangzhou 310027, PR China

Complete contact information is available at:
<https://pubs.acs.org/10.1021/acs.iecr.2c03312>

Notes

The authors declare no competing financial interest.

ACKNOWLEDGMENTS

This work was supported by the Zhejiang Province “Pioneer” R&D Project (grant no. 2022C03040) and the Fundamental Research Funds for the Central Universities (2022ZJFH004, 2021XZZX012).

REFERENCES

- (1) Chindaprasirt, P.; Kampala, A.; Jitsangiam, P.; Horpibulsuk, S. Performance and Evaluation of Calcium Carbide Residue Stabilized Lateritic Soil for Construction Materials. *Case Stud. Constr. Mater.* **2020**, *13*, No. e00389.
- (2) Cong, P.; Mei, L. Using Silica Fume for Improvement of Fly Ash/Slag Based Geopolymer Activated with Calcium Carbide Residue and Gypsum. *Constr. Build. Mater.* **2021**, *275*, 122171.
- (3) Yang, J.; Liu, S.; Ma, L.; Zhao, S.; Liu, H.; Dai, Q.; Yang, Y.; Xu, C.; Xin, X.; Zhang, X.; et al. Mechanism Analysis of Carbide Slag Capture of CO₂ via a Gas-Liquid-Solid Three-Phase Fluidization System. *J. Clean. Prod.* **2021**, *279*, 123712.
- (4) Wang, Y.; Ye, B.; Hong, Z.; Wang, Y.; Liu, M. Uniform Calcite Micro/Nanorods Preparation from Carbide Slag Using Recyclable Citrate Extractant. *J. Clean. Prod.* **2020**, *253*, 119930.
- (5) Li, W.; Huang, Y.; Wang, T.; Fang, M.; Li, Y. Preparation of Calcium Carbonate Nanoparticles from Waste Carbide Slag Based on CO₂ Mineralization. *J. Clean. Prod.* **2022**, *363*, 132463.
- (6) Wang, J.; Cheng, Z.; Hu, Y.; Cao, Y.; Wang, P.; Cao, Z. Depression Behavior and Mechanism of Sodium Silicate on Bastnaesite and Parisite Flotation. *Colloids Surf., A* **2021**, *631*, 127691.
- (7) Sun, L.; Cao, Y.; Liao, Y.; Ma, Z. Interaction Mechanism between Molybdenite and Kaolinite in Gypsum Solution Using Kerosene as the Flotation Collector. *Minerals* **2018**, *8*, 304.
- (8) Xue, Z.; Dong, L.; Fan, M.; Yang, H.; Liu, A.; Li, Z.; Bao, W.; Wang, J.; Fan, P. Enhanced Flotation Mechanism of Coal Gasification Fine Slag with Composite Collectors. *Colloids Surf., A* **2022**, *641*, 128593.
- (9) Cui, L.; Zhao, Z.; Guo, Y.; Cheng, F. Stripping of Iron(III) from Iron(III)-Loaded Aliquat 336 Generated during Aluminum Recovery from Coal Waste Leach Liquor Using Sodium Sulfite. *Sep. Purif. Technol.* **2018**, *199*, 304–310.
- (10) Gao, S. B.; Yue, C. E. J.; Sun, T.; He, D.; Lu, C.; Fu, X. Acid recovering and iron recycling from pickling waste acid by extraction and spray pyrolysis techniques. *J. Clean. Prod.* **2021**, *312*, 127747.
- (11) Xiaofeng, Z.; Yufei, W.; Rui, D.; Xiaoyong, F.; Zhanhui, W. Effect of Coal Gasification Fine Slag Characteristics on Its Floating Carbonization Process. *Henan Chem. Ind.* **2016**, *33*, 11–13.
- (12) Lu, Y.; Wang, X.; Liu, W.; Li, E.; Cheng, F.; Miller, J. D. Dispersion Behavior and Attachment of High Internal Phase Water-in-Oil Emulsion Droplets during Fine Coal Flotation. *Fuel* **2019**, *253*, 273–282.
- (13) Dian, D.; Xuejun, Y.; Zhiquan, P. Flotation-Chemical Method for Treating High-Purity Gypsum with Phosphogypsum. *Non-Met. Mines* **2020**, *43*, 44–48.
- (14) Hu, Z.; Zhang, T.; Lv, L.; Chen, Y.; Zhong, B.; Tang, S. Extraction Performance and Mechanism of TBP in the Separation of Fe³⁺ from Wet-Processing Phosphoric Acid. *Sep. Purif. Technol.* **2021**, *272*, 118822.
- (15) Azizitorghabeh, A.; Rashchi, F.; Babakhani, A. Stoichiometry and Structural Studies of Fe(III) and Zn(II) Solvent Extraction Using D2EHPA/TBP. *Sep. Purif. Technol.* **2016**, *171*, 197–205.
- (16) Vilasó-Cadre, J. E.; Ávila-Márquez, D. M.; Reyes-Domínguez, I. A.; Blanco-Flores, A.; Gutiérrez-Castañeda, E. J. Coal Flotation in a Low-Rank Carbonaceous Mineral Using 3-Phenyl-1-Propanol as a Collector Reagent. *Fuel* **2021**, *304*, 121363.
- (17) Zhu, X. n.; Wang, D. z.; Ni, Y.; Wang, J. x.; Nie, C. c.; Yang, C.; Lyu, X. j.; Qiu, J.; Li, L. Cleaner Approach to Fine Coal Flotation by Renewable Collectors Prepared by Waste Oil Transesterification. *J. Clean. Prod.* **2020**, *252*, 119822.
- (18) Cui, L.; Li, S.; Kang, J.; Yin, C.; Guo, Y.; He, H.; Cheng, F. A Novel Ion-Pair Strategy for Efficient Separation of Lithium Isotopes Using Crown Ethers. *Sep. Purif. Technol.* **2021**, *274*, 118989.
- (19) He, P.; Zhang, X.; Peng, X.; Jiang, X.; Wu, J.; Chen, N. Interaction of Elemental Mercury with Defective Carbonaceous Cluster. *J. Hazard. Mater.* **2015**, *300*, 289–297.
- (20) Huang, Y.; Cheng, Q.; Wang, Z.; Liu, S.; Zou, C.; Guo, J.; Guo, X. Competitive Adsorption of Benzene and Water Vapor on Lignite-Based Activated Carbon: Experiment and Molecular Simulation Study. *Chem. Eng. J.* **2020**, *398*, 125557.
- (21) Hou, M.; Cen, W.; Zhang, H.; Liu, J.; Yin, H.; Wei, F. Adsorption and oxidation of NO on graphene oxides: A dispersion corrected density functional theory investigation. *Appl. Surf. Sci.* **2015**, *339*, 55–61.
- (22) Zhang, L.; Guo, J.; Xie, Z.; Li, B.; Liu, S. Micro-Mechanism of Improving Low-Rank Coal Flotation by Using Carboxylic Acid Collector: A DFT Calculation and MD Simulation Study. *Colloids Surf., A* **2021**, *622*, 126696.
- (23) Ling, Y.; Li, J.; Zou, C.; Wu, J.; Zhao, P.; Xie, X.; Qi, Y.; Liu, Q.; Hong, J.; Li, S. Interaction Mechanism between Gaseous Arsenic and the Unburned Carbon in Coal-Fired Fly Ash: A DFT Combined Thermodynamics Study. *Chem. Eng. J.* **2021**, *425*, 130714.
- (24) Miehlich, B.; Savin, A.; Stoll, H.; Preuss, H. Results Obtained with the Correlation Energy Density Functionals of Becke and Lee, Yang and Parr. *Chem. Phys. Lett.* **1989**, *157*, 200–206.
- (25) Weigend, F.; Ahlrichs, R. Balanced Basis Sets of Split Valence, Triple Zeta Valence and Quadruple Zeta Valence Quality for H to Rn: Design and Assessment of Accuracy. *Phys. Chem. Chem. Phys.* **2005**, *7*, 3297–3305.
- (26) Su, L.; Pan, B.; Sun, Z.; Song, P.; Song, X. Extraction Kinetics of Nitric Acid from the Nitric Acid-Hydrochloric Acid-Potassium Chloride Solution by Tributyl Phosphate. *Sep. Purif. Technol.* **2021**, *274*, 118984.
- (27) Fan, J.; Wang, G.; Xu, S.; Zhu, J.; Zhang, J.; Chen, J.; Zheng, L.; Pan, J.; Wang, R.; Hao, Y. Removal of Impurities from Bismuth Pickling Solution Using Solvent Extraction with TBP. *Hydrometallurgy* **2022**, *207*, 105779.
- (28) Cui, L.; Wang, L.; Feng, M.; Fang, L.; Guo, Y.; Cheng, F. Ion-Pair Induced Solvent Extraction of Lithium (I) from Acidic Chloride Solutions with Tributyl Phosphate. *Green Energy Environ.* **2021**, *6*, 607–616.
- (29) Pietrzak, R.; Wachowska, H. The Influence of Oxidation with HNO₃ on the Surface Composition of High-Sulphur Coals: XPS Study. *Fuel Process. Technol.* **2006**, *87*, 1021–1029.
- (30) Ding, X.; Jiao, W.; Yang, Y.; Zeng, Z.; Huang, Z. Effects of Oxygenated Groups on the Adsorption Removal of Dibenzofuran by Activated Coke: Experimental and DFT Studies. *J. Environ. Chem. Eng.* **2021**, *9*, 106775.
- (31) Liu, Z.; Wu, Z.; Zheng, Z.; Wang, X.; Guedes Soares, C. G. Modelling Dynamic Maritime Traffic Complexity with Radial Distribution Functions. *Ocean Eng.* **2021**, *241*, 109990.
- (32) Han, Y.; Liu, W.; Zhou, J.; Chen, J. Interactions between kaolinite Al OH surface and sodium hexametaphosphate. *Appl. Surf. Sci.* **2016**, *387*, 759–765.
- (33) Ribeiro, I. H. S.; Reis, D. T.; Pereira, D. H. A DFT-Based Analysis of Adsorption of Cd²⁺, Cr³⁺, Cu²⁺, Hg²⁺, Pb²⁺, and Zn²⁺, on Vanillin Monomer: A Study of the Removal of Metal Ions from Effluents. *J. Mol. Model.* **2019**, *25*, 267.
- (34) Yin, Q.; Si, L.; Wang, R.; Zhao, Z.; Li, H.; Wen, Z. DFT Study on the Effect of Functional Groups of Carbonaceous Surface on Ammonium Adsorption from Water. *Chemosphere* **2022**, *287*, 132294.